Control of Magnetization Dynamics in $Ni_{81}Fe_{19}$ Thin Films Through the Use of Rare-Earth Dopants

William Bailey, Pavel Kabos, Frederick Mancoff, and Stephen Russek

***Abstract*—We show that the magnetization dynamics of soft ferromagnetic thin films can be tuned using rare-earth (RE) dopants. Low concentrations (2 to 10%) of Tb in 50 nm $Ni_{81}Fe_{19}$ films are found to increase the Gilbert magnetic damping parameter α over two orders of magnitude without great effect on easy axis coercivity or saturation magnetization. Comparison with Gd dopants indicates that the orbital character of the Tb moment is important for transferring magnetic energy to the lattice. Structural transformations from the crystalline to the amorphous state, observed over the first 2%–10% of RE doping, may play a contributing but not sufficient role in damping in these films. The approach demonstrated here shows promise for adjusting the dynamical response, from underdamped to critically damped, in thin film materials for magnetic devices**

***Index Terms*—Magnetization dynamics, Ni–Fe alloys, rare-earth.**

I. Introduction

THE DYNAMICAL response of film magnetization to short (picosecond) field pulses is an essential question for magnetic thin-film device technology. In both read and write elements of magnetic recording heads and in the switching elements of magnetic random access memory (M-RAM) devices, ever-shorter time scales are becoming relevant for attaining higher data rates (>100 Mbyte/s). The dynamical response of typical films used in these devices, notably permalloy ($Ni_{81}Fe_{19}$), has been studied fairly intensively in the last several years [1]–[4].

From a materials science and engineering point of view, however, little experimental work exists on *tailoring* the dynamical response of thin 3d ferromagnet metal films (Fe, Ni, Co). This contrasts with the situation for insulating ferromagnets such as the garnets, which have been of interest for microwave applications for many years. It has been known for decades that as little as 0.1% of rare-earth impurities can completely dominate the microwave linewidth ΔH of yttrium iron garnet (YIG) [5]. Tb, in particular, is known to have the strongest effect of all rare-earth impurities [6]. It is natural to examine the rare-earths as starting points for a study on dynamics in 3d-ferromagnets.

Manuscript received October 13, 2000.

The work of W. Bailey and F. Mancoff was supported by NRC postdoctoral fellowships.

W. Bailey is now with the Materials Science Division, Department of Applied Physics, Columbia University, New York, NY 10027 USA (e-mail: web54@columbia.edu).

P. Kabos, F. Mancoff, and S. Russek are with the National Institute of Standards and Technology (NIST), Division 814, Boulder, CO 80305 USA.

Publisher Item Identifier S 0018-9464(01)06314-2.

II. Background

The basic formalism for magnetic dynamics is the Landau–Lifshitz–Gilbert equation:

$$\frac{d\mathbf{M}}{\mathbf{dt}} = -\,|\,\gamma\,|\,(\mathbf{M}\times\mathbf{H}_{\text{eff}}) + \frac{\alpha}{M_s}\left(\mathbf{M}\times\frac{\mathbf{dM}}{\mathbf{dt}}\right). \quad (1)$$

The first term describes the precession of the magnetization about the effective field and the second term describes its dissipation. The constant γ is the gyromagnetic ratio, $\mathbf{H}_{\text{eff}}$ is the effective field on the sample with applied, demagnetization, and anisotropy contributions, and M_s is the saturation magnetization. The dissipation, or magnetic damping, is described by the dimensionless constant α.

The magnetic damping α manifests itself straightforwardly in ultrafast measurements of magnetization dynamics. For thin films under step-field pulses in the film plane, under the assumption of single-particle Stoner-Wolfarth behavior, and for small displacement angles and damping, the LLG equation reduces to

$$\phi(t) = \phi_o + \beta_o e - \left[\left(\frac{1}{2}\gamma\mu_o M_s\right)\alpha t\right]\sin(\omega_p t + \varphi), \quad (2)$$

where

- ϕ is the angle of $\mathbf{M}$ in the film plane and
- ϕ_o its equilibrium value, and
- ω_p is the precessional frequency, typically 2–4 GHz in soft ferromagnetic films such as $Ni_{81}Fe_{19}$ [7].

The magnetic relaxation is thought to arise from several possible microscopic mechanisms. If $\mathbf{M}$ is driven in the uniform mode, in which all spins rotate with equal phase and angle across the sample, this corresponds to the $\mathbf{k}=0$ magnon with related angular momentum and energy. In relaxation, both angular momentum and energy of this magnon must be transferred out of the spin system and into the lattice (phonons). Ultimate coupling of the magnetic moments, which are spin moments in $Ni_{81}Fe_{19}$ alloys, to the lattice is believed to be effected through the spin-orbit coupling. However, higher-order processes can mediate the coupling, and the relaxation may proceed first into shorter-wavelength magnons. [5]

Experimentally, microscopic understanding is best developed in the case of the ferrites. Indirect coupling is generally believed to be responsible for damping in the case of disordered materials, either with volume pits or finite crystallite size. Direct coupling is believed to be responsible for the damping for rare-earth dopants in YIG. In this case, the angular momentum and energy may be transferred directly to the local moment on the rare-earth site. Recent work in this area has been performed by Dionne and Finch [8]. A hallmark for the direct coupling mechanism is

a peak in the damping (expressed as linewidth ΔH) observed around 80 K, with a $1/T$ dependence at higher temperatures.

III. Experimental Method

The main purpose of the study is to examine the effects of rare-earth doping on the magnetic damping α of permalloy films. Concurrent effects of doping on the static magnetic properties saturation magnetization $M_{\rm sat}$, coercivity H_c, and anisotropy field H_k have also been measured. Covariation of microstructure, particularly the amorphization of polycrystalline $Ni_{81}Fe_{19}$ films through the addition of rare-earth dopants, has been monitored by X-ray diffraction.

A. Sample Preparation

All samples were prepared by DC magnetron sputtering in a magnetic field. Permalloy-rare earth alloys $(Ni_{81}Fe_{19})_{100-x}RE_x$ were formed by cosputtering a $Ni_{80}Fe_{20}$ alloy target with an elemental rare earth (Tb or Gd) target, located at diagonal points of a confocal cluster of four sputter sources.

Three series of permalloy-rare earth alloys were prepared, $0 \leq x \leq 20\%$. *Series A* and *Series B* are Tb-doped, sputtered at different Ar pressures, $P_{Ar} = 1.2$ Pa (9.0 mTorr) for series A and $P_{Ar} = 0.66$ Pa (5.0 mTorr) for series B. The purpose here is to explore a secondary microstructural dependence of $\alpha(X_{\rm Tb})$, and more importantly, to examine effects of doping on optimized $Ni_{81}Fe_{19}$. Lowest sputtering pressure and highest sputtering power have been found to produce the best soft magnetic properties in our chamber; $P_{Ar} = 0.66$ Pa (5.0 mTorr) is the lowest pressure for which the plasma is sustainable. In *Series C*, Gd was added at $P_{Ar} = 0.66$ Pa (5.0 mTorr). Compositions were determined from the relative flux rates of the two sputtering sources, as determined from deposition rates measured at a crystal monitor.

B. Microstructural Characterization

Crystallinity for the three series of films was investigated by X-ray diffraction using Cu $K\alpha$ radiation from a sealed anode. Initial azimuthal alignment was controlled to 0.2°, and four-circle control allowed investigation of orientational effects. High diffracted intensities were available through a close anode-sample spacing (3 cm) and broad spherical slits (2 mm) at the source and detector. Scans were focused around the (111) peak of $Ni_{81}Fe_{19}$ between 42–46° in 2θ, in the symmetric scattering geometry.

A secondary indication of microstructure has been found through four-point resistivity measurements. In this case, an inline probe with 1 mm spacing was centered on the sample, and the standard geometric correction factor was applied.

C. Magnetic Characterization

1) Statics: The static magnetic properties of the samples were investigated using alternating gradient, induction-field B-H looper, and SQUID magnetometry. Estimates of easy-axis coercivity H_c are taken from alternating-gradient magnetometry (AGM) measurements; estimates of anisotropy fields in the hard axis H_k are taken from looper measurements, due to greater ease in finding the exact hard-axis orientation off of nominal. H_c estimates agree well between AGM and looper measurements. Room-temperature saturation magnetization $M_{\rm sat}$ was measured as a function of composition using the AGM. AGM samples were diced using a wafer saw to a standard size (3 mm $\times$ 6 mm) to remove geometrical effects. $M_{\rm sat}$ vs. temperature has been recorded for some samples from series B using a SQUID magnetometer down to 10 K.

2) Dynamics: The dynamical response of the film magnetization to ultrafast step-pulses was investigated using a time-domain microwave inductive technique. The technique is described in detail in [7]; some general features are summarized here.

The magnetic film, coated with photoresist, is placed on a microwave coplanar waveguide which is connected in transmission between a step pulse generator and a sampling oscilloscope. When a step current pulse was generated and passes by the film, it produces a fringing field which rotates the film magnetization orthogonal to the waveguide. Risetime for the field step is 150 ps, and the step duration is 10 ns. The field step is fairly small, only $\simeq 0.16$ kA/m (2 Oe) in magnitude.

The motion of $\mathbf{M}$ produces an inductive voltage in the waveguide which sums with the resistive voltage from the transmitted current pulse. To remove the resistive contribution, the transmitted waveform at a saturating colinear magnetic field, for which no motion is expected, is subtracted. The net signal is proportional to dM/dt in the direction orthogonal to the waveguide. Temperature-dependent measurements were taken using a cryogenic probe station with microwave feedthroughs and open-loop liquid He cooling.

IV. Experimental Results

The experimental results are grouped in three sections. In Section IV-A, we show the effects of Tb and Gd dopants on the magnetic damping. Tb impurities are shown to have a strong effect on the damping whereas Gd impurities do not. The damping contribution from Tb is strongly temperature dependent, decreasing with increasing temperature, and there is an apparent matrix dependence on the strength of damping contributed per Tb atom. In Section IV-B, concurrent effects on soft magnetic properties $M_{\rm sat}$, H_k, and H_c are examined through B-H looper and AGM measurements. These vary among the series but are generally not large at low concentrations. Finally, microstructural effects accompanying the addition of dopants are explored in Section V.

A. Magnetic Dynamics

The effects of rare-earth dopants on magnetization dynamics are shown first. Time-domain voltage waveforms of the inductive measurement are shown in Fig. 1, for the first several points of the Tb-doped Series A. Fits to the integrated LLG equation (not (2)) and extractions of the damping constant α are shown alongside the data. It may be seen that the agreement between experiment and the model is rather good, except in the case of longer times for the undoped sample. In this case, there is some apparent drift in the precessional frequency ω.

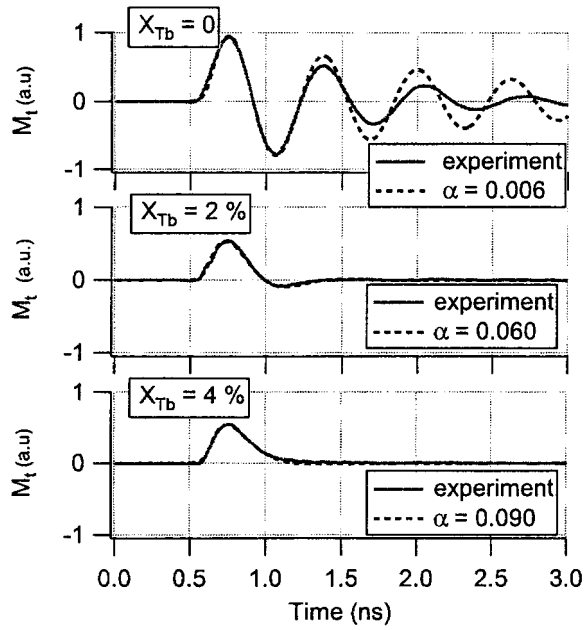

Fig. 1. Inductive measurement of transverse magnetization dynamics, with LLG fits, for increasing Tb doping of Series A. Measurements are taken at room temperature.

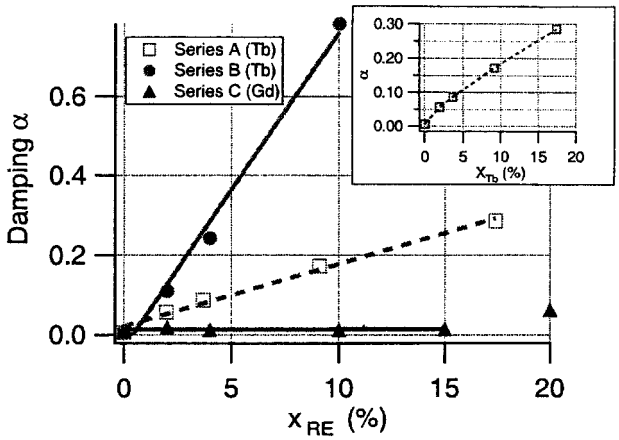

Fig. 2. Magnetic damping parameter α for the three series in rare-earth doping. Series A: Tb at 1.2 Pa (9.0 mTorr) Ar, Series B: Tb at 0.66 Pa (5.0 mTorr) Ar, Series C: Gd at 0.66 Pa (5.0 mTorr) Ar. See text for details. Measurements are taken at room temperature. Inset: expanded scale for Tb Series A.

A plot of the damping parameter α vs. Tb-doping fraction f_{Tb} for the same series is shown in Fig. 2 (inset). It may be seen that α increases by a factor of 50 over the full doping series, and by an order of magnitude with just 2% Tb added. The magnetic dynamics proceed in this series from underdamped at 0%, to critically damped at 2%, to overdamped at 4%.

Fitted values of α for all three series of rare-earth doped samples are summarized in Fig. 2. A much larger response in α to composition is observed for the Tb-doped series B compared with the Tb-doped series A. It is evident, on the other hand, that the Gd-doped series exhibits little systematic trend on the damping even for concentrations out to 15%. α for this series remains low at $\simeq 0.01$.

There is a marked temperature dependence for the damping contributed by Tb dopants. Fig. 3 shows extracted values

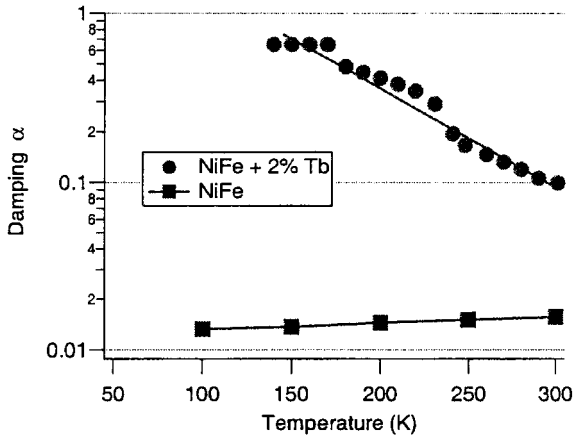

Fig. 3. Temperature dependence of damping $\alpha(T)$ found through cryogenic inductive measurements. Note the opposing trends for the undoped and Tb-doped samples.

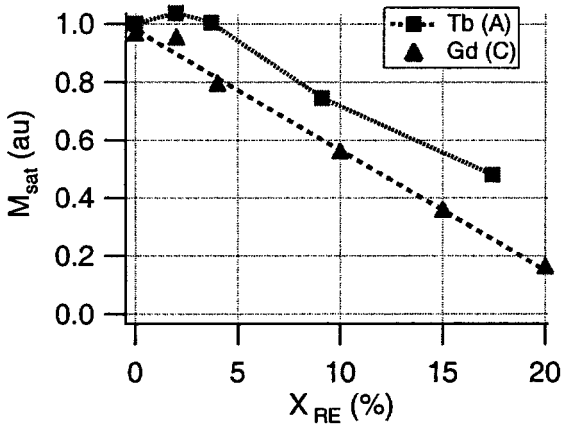

Fig. 4. Saturation magnetization, normalized to the amount of $Ni_{81}Fe_{19}$ in the film, for the Tb-doped Series A and the Gd-doped Series C. as measured by AGM.

of α for cryogenic inductive measurements. While undoped $Ni_{81}Fe_{19}$ shows a small decrease in α during cooling to 100 K, the sample with 2% Tb (from Series B) increases in damping quite strongly. α is seen to rise from 0.1 at room temperature to 0.6 at 150 K. Some nonlinearity is present in the temperature dependence, with apparent discontinuities at 230 K and 170 K. Fits cease to be reliable for temperatures below 140 K, as the dynamics become more and more strongly overdamped. Permalloy, on the other hand, shows only decreasing damping as a function of temperature, roughly linear to 100 K.

B. Static Magnetic Properties

Saturation magnetization M_{sat} as a function of doping is shown in Fig. 4. The data are shown in two different ways. The measured moments are normalized to the total amount of $Ni_{81}Fe_{19}$ deposited in the sample. Deposition rates for $Ni_{81}Fe_{19}$ and RE are assumed to sum in this case.

For the normalization to $Ni_{81}Fe_{19}$ moments, a slight (5%) initial increase appears to be present for the Tb-doped case over the first 2% of doping. The Gd-doped samples, on the other hand, show a mostly monotonic and linear decrease, matched by the Tb-doped samples for $x_{\mathrm{Tb}} > 4\%$. The Tb curve takes a different

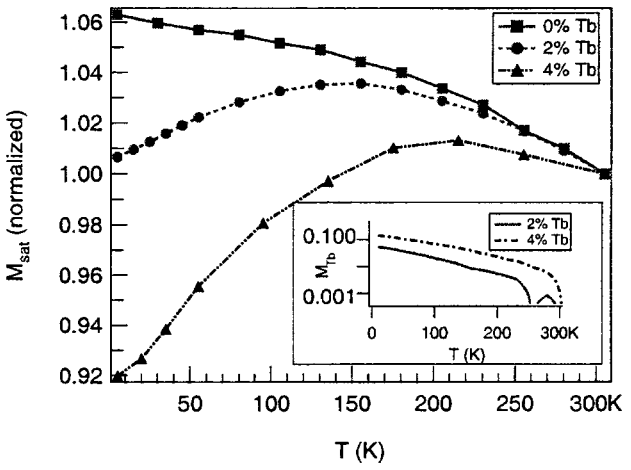

Fig. 5. Temperature dependence of saturation magnetization for low Tb doping (0, 2, and 4%). *Inset:* Contribution of Tb dopants M_{Tb} as a function of temperature, see text for details. A roughly exponential increase of the Tb-related magnetization, opposing the $Ni_{81}Fe_{19}$ magnetization, with decreasing temperature is present. Note the similarity in T dependence with that in Fig. 3.

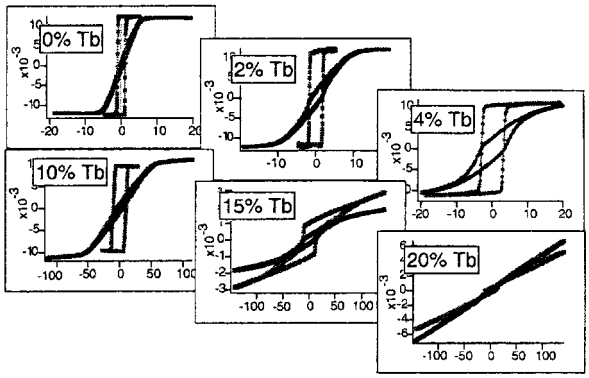

Fig. 6. Hard-axis and easy-axis loops for the Tb-doped Series B. Vertical axes are moment in arbitrary units; horizontal axes are magnetic field in multiples of 79.6 A/m (Oe). Note the change in field scale between the first and second row.

form from the thickness-normalized curve, which is flat at low doping. For the Gd-doped series, total deposition time has been held constant, so this correction has been applied during growth.

The temperature dependence of M_{sat} for the Tb-doped series B is shown in Fig. 5, as measured by SQUID magnetometry. Moments in this case are normalized to each sample's value at 305 K, due to unresolved questions with calibration. Undoped permalloy displays the expected approach to maximum value at low temperature. The 2% and 4% Tb-doped samples, on the other hand, display a maximum in M_{sat} with increasing temperature; the temperature position of this maximum increases with increasing Tb content. This decrease in M_{sat} is consistent with the idea that RE moments align antiparallel with $Ni_{81}Fe_{19}$ moments. If the contribution of the Tb dopants to total magnetization is isolated by subtracting the temperature dependence of $Ni_{81}Fe_{19}$ only, an exponential increase with equal activation energy for the 2% and 4% cases becomes evident.

Loop shapes for the Tb-doped Series B, as measured by B-H looper magnetometry, are shown in Fig. 6. Easy- and hard-axis loops are plotted together. In the undoped case, the magnetic

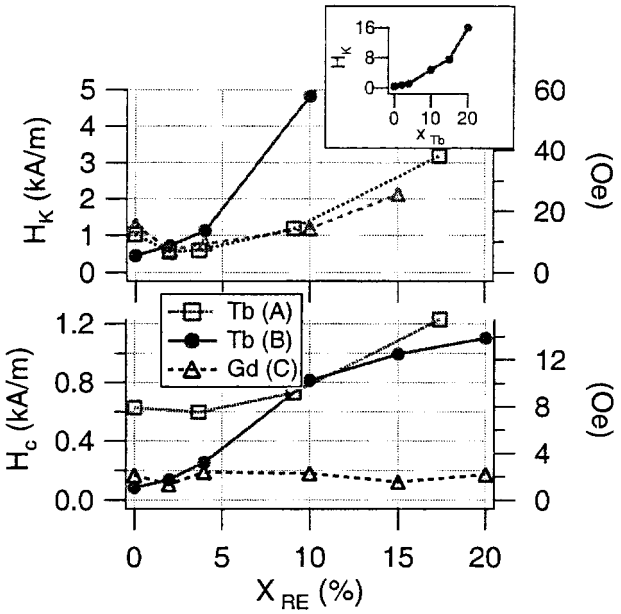

Fig. 7. Easy-axis coercivity H_c and hard-axis anisotropy field H_k for the three rare-earth doped series A to C. *Inset:* H_k in kA/m for the Tb-doped Series B.

properties approximate ideal easy- and hard-axis loop shapes fairly closely, with high coercive squareness along the easy-axis and near-zero remanence along the hard-axis. These properties are retained for the 2% and 4% Tb-doped samples. With increasing doping to 10% Tb, the easy axis squareness remains high, but coercivity H_c increases to 0.8 kA/m (10 Oe.) The hard axis properties retain linearity, but with increasing anisotropy fields H_k to 4.0 kA/m (50 Oe) by 10% Tb. Above 10% Tb, a transition to perpendicular anisotropy may be inferred, as both in-plane loops take hard-axis character.

The magnetic properties H_k and H_c for the three series are summarized in Fig. 7. For the question of optimization of damping with soft magnetic properties, the Tb-doped series B samples are most relevant, as the starting properties are best and effects on damping most pronounced in this case. We find that from 0 to 4% addition of Tb, H_k rises from 0.45 to 1.13 kA/m (5.7 to 14.2 Oe), and H_c rises from 80 to 246 A/m (1.0 to 3.1 Oe). From 10% Tb and beyond, anisotropy fields increase rapidly (see inset), and the coercivity curve begins to turn over, reaching a maximum of $\simeq$ 1 kA/m. Both of these features are consistent with the formation of perpendicular anisotropy with increasing Tb content.

It is interesting to note that the compositional dependence of H_k is quite similar for both the Tb-doped series A and the Gd-doped series C. An initial *decrease* in anisotropy field is present, followed by a slight increase. Similarly, H_c shows an initial decrease for the Tb-doped series B from 0.62 kA/m (7.8 Oe.) It is possible that a structural transformation over $0 < x_{\mathrm{RE}} < 10\%$ is responsible for the magnetic properties in this range. On the other hand, H_c for the Gd doped sample is substantially constant over the full range of doping, to 20%.

V. Microstructure

Film resistivities vs. impurity fraction are shown in Fig. 8. As expected, there is an increasing trend in resistivity with

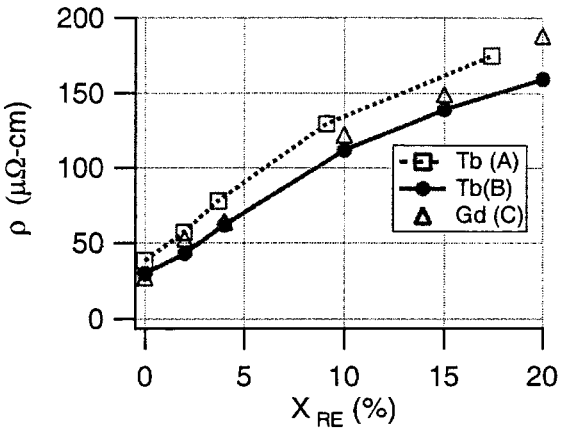

Fig. 8. Measured film resistivities for the Tb-doped samples. Note the very rapid rise in resistivity from $0 < X_{\rm RE} < 10\%$, and the greater values measured for Series A compared with Series B.

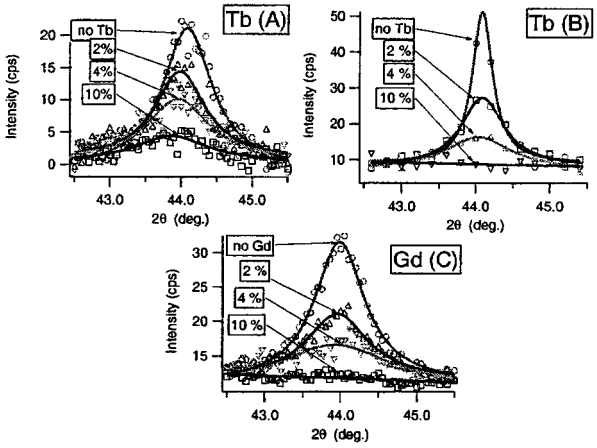

Fig. 9. XRD scans of the $Ni_{81}Fe_{19}$ (111) peak for the three doping Series A–C. Both Tb and Gd dopants produce a crystalline to amorphous transformation which is complete at 10%. The lines are Lorentzian peak fits for the 2θ values plotted.

increasing impurity content. However, several interesting features are present.

First, the impurity resistivities contributed by RE dopants in $Ni_{81}Fe_{19}$ are substantially higher than may be expected for substitutional impurities in a metallic host. Roughly 10 $\mu\Omega$ cm/% is added to $Ni_{81}Fe_{19}$ with Gd and Tb dopants up to $X_{\rm RE} =$ 10%. Tabulated values in the Landölt-Bornstein tables generally do not exceed 6–7 $\mu\Omega$ cm/% [9]. Secondly, there is roughly a 15 $\mu\Omega$ cm difference between values measured for the Tb series A and Tb series B. Series B values are generally lower, and matched by those found in Series C.

The resistivity data are understandable through X-ray diffraction measurements. We find that the crystallinity of the $Ni_{81}Fe_{19}$ films is destroyed through the addition of Tb and Gd rare-earth dopants. Fig. 9 shows (111)-peak intensity plots for the three series A–C as Tb and Gd dopants are added to the lattice. A progressive broadening of the peak width and reduction of the peak height with increasing RE concentration may be observed. For Tb dopants in Series A, there is a shift of the (111) to higher d-spacing and lower angle with increasing concentration. This straining is not present for series B or C.

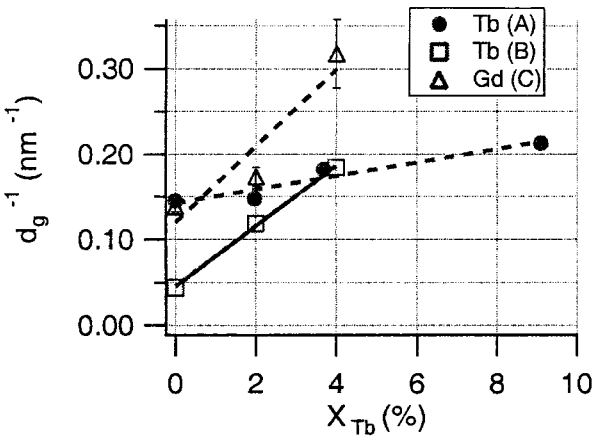

Fig. 10. Grain size estimates for the three RE doping series, plotted as $(1/d_g)$. The increasing trend in inverse grain size is an indication of amorphization in the structure. Note that the least rapid amorphization proceeds in Tb-doped series B, Gd-doped and Tb-doped series A being roughly equal. Compare with rates of α increase in Fig. 2.

Using the width of the fitted Lorentzian peak, grain sizes have been estimated in the film normal direction through the Debye-Scherer formula. A correction has been applied to account for the finite width of the detector slits. Inverse grain size as a function of RE content is shown in Fig. 10.

VI. Discussion

The comparison between Gd and Tb dopants in $Ni_{81}Fe_{19}$ films provides some indication of the damping mechanism which has been manipulated in these films. Gd dopants produce no effect on damping, whereas Tb dopants increase the damping strongly, as shown in Fig. 2. On the other hand, both types of dopants have the same effect of microstructural transformation; that is, both amorphize the sample at roughly the same rate, as indicated by the slope of inverse grain diameter $1/d_g$ vs. $X_{\rm RE}$ in Fig. 10. We may conclude from this observation that destruction of the crystal lattice alone is insufficient to produce the observed large damping in thin-film $Ni_{81}Fe_{19}$.

Gd and Tb dopants provide an interesting comparison since they differ principally in the nature of their local moment. Similar to the case for all the rare earths, the magnetic properties of these two elements, adjacent in the rare earth series, are controlled by the tightly localized $4f$ shell. Similar magnetic moments are observed for the rare earths whether present as ions in compounds or in metals. For Gd, however, the whole of the magnetic moment is due to spin, where Tb has equal parts arising from spin and orbital angular momentum [10].

The $M_{\rm sat}(T)$ for Tb-doped and $M_{\rm sat}(X_{\rm RE})$ data for Tb and Gd-doped $Ni_{81}Fe_{19}$ (Figs. 4 and 5) are consistent with the idea that RE moments align antiparallel to the $Ni_{81}Fe_{19}$ magnetization. We find that the excess magnetization with Tb doping (inset, Fig. 5) is strongly temperature dependent, falling off exponentially with increasing temperature as $M_{\rm Tb} = A\exp(-\beta T)$.

A similar temperature dependence as that found for $M_{\rm Tb}(T)$ is observed for $\alpha(T)$ for 2% Tb doping (see Fig. 3). The falloff is more rapid than the T^{-1} dependence found for relaxation due to RE dopants in YIG, being best approximated

in this case by T^{-3}. If the Tb-dependent part of $M_{\rm sat}(T)$ (inset, Fig. 5) is identified with magnetization on Tb sites, and their temperature-dependent magnetization identified with a temperature-dependent antiferromagnetic coupling of Tb moments to the $Ni_{81}Fe_{19}$ spin system, the two results are consistent with a direct damping mechanism to the lattice. Tb moments, coupled to the lattice through their orbital moment, may relax the magnetization more effectively at lower temperature when the spins are more tightly bound to them. Gd spin moments, on the other hand, are not coupled to the lattice, so no damping is produced by them.

The microstructural dependence of damping in Tb-doped samples is an open question. We observe that damping, while roughly proportional to $x_{\rm RE}$ in this case, does not at all show the same proportionality constant in Series A and B, Series B increasing in α roughly three to four times more quickly. This is matched by a three to four times more rapid rate of amorphization in Series B compared with Series A (Fig. 10). It is possible that the increased crystallographic disorder provides an additional indirect (two-magnon) path to the lattice. However, no sum of $x_{\rm Tb}$ and $1/d_g(x_{\rm Tb})$ terms fits the experimental dependence of α on $x_{\rm Tb}$ for the two cases.

VII. Conclusions

We have demonstrated a method to tune the magnetic dynamic relaxation in soft device materials, while retaining the important soft magnetic properties. To our knowledge, prior efforts in this area do not exist. Comparison of Tb and Gd dopants indicates that some orbital spin moment may be necessary for increasing relaxation. We hope that these results will stimulate further interest in engineering the magnetic dynamics of thin-film magnetic device materials.

Acknowledgment

W. Bailey thanks Türgut Gur at the Laboratory for Advanced Materials at Stanford University for graciously allowing use of the "Picker" x-ray diffractometer. S. Russek would like to acknowledge helpful discussions with J. Slonczewski.

References

[1] R. Koch, G. Grinstein, G. Keefe, Y. Lu, P. Troulloud, W. Gallagher, and S. Parkin, "Thermally assisted magnetization reversal in submicron-sized magnetic thin films," *Phys. Rev. Lett.*, vol. 84, pp. 5419–5422, June 2000.

[2] S. E. Russek, S. Kaka, and M. J. Donahue, "High-speed dynamics, damping, and relaxation times in submicrometer spin-value devices," *J. Appl. Phys.*, vol. 87, pp. 7070–3, May 2000.

[3] T. Crawford, T. Silva, C. Teplin, and C. Rogers, "Subnanosecond magnetization dynamics measured by the second-harmonic magneto-optic kerr effect," *Appl. Phys. Lett.*, vol. 74, pp. 3386–8, May 1999.

[4] C. Back, R. Allenspach, W. Weber, S. Parkin, D. Weller, E. Garwin, and H. Siegmann, "Minimum field strength in precessional magnetization reversal," *Science*, vol. 285, pp. 864–7, August 1999.

[5] M. Sparks, *Ferromagnetic-relaxation theory*: McGraw-Hill, 1964.

[6] J. Dillon and J. Nielsen, "Ferrimagnetic resonance in rare-earth doped yttrium iron garnet," *Physical Review*, vol. 120, no. 105, August 1960.

[7] T. Silva, C. Lee, T. Crawford, and C. Rogers, "Inductive measurement of ultrafast magnetization dynamics in thin-film permalloy," *J. Appl. Phys.*, vol. 85, pp. 7849–62, June 1999.

[8] G. F. Dionne and G.L. Finch, "Temperature dependence of spin-lattice relaxation in rare-earth iron garnets," *J. Appl. Phys.*, vol. 87, pp. 4963–6, May 2000.

[9] J. Bass, "Landolt-Bornstein Tables," in *Metals: Electronic Transport Phenomena*, J. Bass, Ed: Dusseldorf: Springer-Verlag, 1990, ch. III-3, sec. 1.4, pp. 166–178.

[10] S. Chikazumi and S. Charap, *Physics of Magnetism*: John Wiley and Sons, 1964.